

DRAFT VERSION JANUARY 19, 2022
Typeset using L^AT_EX **modern** style in AASTeX62

The misaligned orbit of the Earth-sized planet Kepler-408b

SHOYA KAMIKA,¹ OTHMAN BENOMAR,² YASUSHI SUTO,^{1,3} FEI DAI,^{4,5}
KENTO MASUDA,^{5,6} AND JOSHUA N. WINN⁵

¹*Department of Physics, The University of Tokyo, Tokyo, 113-0033, Japan*

²*Center for Space Science, NYUAD Institute, New York University Abu Dhabi, PO Box 129188, Abu Dhabi, UAE*

³*Research Center for the Early Universe, School of Science, The University of Tokyo, Tokyo 113-0033, Japan*

⁴*Department of Physics and Kavli Institute for Astrophysics and Space Research, Massachusetts Institute of Technology, Cambridge, MA 02139, USA*

⁵*Department of Astrophysical Sciences, Princeton University, Princeton, NJ 08544, USA*

⁶*NASA Sagan Fellow*

(Received 2018 November 23; Revised 2019 February 1; Accepted 2019 February 5)

Submitted to AJ

ABSTRACT

Kepler-408 is one of the 33 planet-hosting *Kepler* stars for which asteroseismology has been used to investigate the orientation of the stellar rotation axis relative to the planetary orbital plane. The transiting “hot Earth,” Kepler-408b, has an orbital period of 2.5 days and a radius of $0.86 R_{\oplus}$, making it much smaller than the planets for which spin-orbit alignment has been studied using the Rossiter-McLaughlin effect. Because conflicting asteroseismic results have been reported in the literature, we undertake a thorough re-appraisal of this system and perform numerous checks for consistency and robustness. We find that the conflicting results are due to the different models for the low-frequency noise in the power spectrum. A careful treatment of the background noise resolves these conflicts, and shows that the stellar inclination is $i_{\star} = 42^{+5}_{-4}$ degrees. Kepler-408b is, by far, the smallest planet known to have a significantly misaligned orbit.

Keywords: asteroseismology — stars: oscillations — stars: rotation — stars: planetary systems — methods: data analysis — techniques: photometric

Corresponding author: Yasushi Suto
suto@phys.s.u-tokyo.ac.jp

1. INTRODUCTION

Planets around other stars are occasionally found to have orbits that are misaligned, or even retrograde, relative to the direction of stellar rotation (e.g., Winn & Fabrycky 2015; Triaud 2017). However, all previous detections of misaligned orbits are for planets larger than Neptune. Smaller planets are relatively unexplored because of the difficulty of the relevant measurements.

Three of the techniques for investigating spin-orbit alignment — the Rossiter-McLaughlin effect, the starspot-tracking method, and the gravity-darkening method — require the observation of signals for which the amplitude is proportional to the loss of light during planetary transits. Hence, they are much easier to apply to giant planets than small planets. Two other techniques — the asteroseismic method, and the $v \sin i$ method — rely on observing signals that are independent of planet size. However, the asteroseismic method has only been applied to 33 stars, because it requires an unusually bright star with large-amplitude p -mode oscillations. The $v \sin i$ method has been applied to samples of hundreds of stars, but in most cases it only provides weak constraints (Schlaufman 2010; Winn et al. 2017). Due to these limitations, it is unclear whether the misalignments are the result of processes specific to giant planets, or whether they also occur for terrestrial planets.

Kepler-408 (also known as KIC 10963065 and KOI-1612) is one of approximately 150,000 Sun-like stars that were monitored for 4 years with the NASA *Kepler* space telescope (Borucki et al. 2010). Its lightcurves exhibit a periodic transit signal due to an Earth-sized planet with $P_{\text{orb}} \sim 2.5$ days (Marcy et al. 2014). Table 1 summarizes the known characteristics of the system. With a *Kepler* apparent magnitude of 8.8, the host star is the third brightest of all the *Kepler* stars with confirmed planets. This unusual brightness enables an investigation of the stellar obliquity using asteroseismology. In particular, it is possible to determine the inclination i_* of the stellar rotation axis based on the fine structure in the p -mode pulsation spectrum (Toutain & Gouttebroze 1993; Gizon & Solanki 2003).

However, there are conflicting reports in the literature. Campante et al. (2016) found the inclination to be consistent with 90° and set a lower limit of 54° . This was part of a homogeneous study of 25 stars with transiting planets. In contrast, Nielsen et al. (2017) found the inclination to be between 40 and 45 degrees. This finding was incidental to the main purpose of the study, which was to probe the internal rotation profiles of 6 stars. The authors did not remark on the transiting planet, nor on the conflict with Campante et al. (2016).

We have examined the case of Kepler-408 in greater detail, to try and resolve this conflict. We were also motivated by the numerical simulations of Kamiaka et al. (2018), who established the observational requirements for the reliable inference of the rotational inclination, and found that the characteristics of Kepler-408 should allow for reliable results. Section 2 describes the transit analysis. Section 3 presents some independent checks on the previous measurements of the stellar rotation period, which

Table 1. System Parameters of Kepler-408

Parameter	Value	Reference
<i>Stellar Parameters</i>		
Effective temperature, T_{eff} [K]	6088 ± 65	Petigura et al. (2017)
Surface gravity, $\log(g/\text{cm s}^{-2})$	$4.318^{+0.08}_{-0.089}$	Petigura et al. (2017)
Metallicity, [Fe/H]	$-0.138^{+0.043}_{-0.042}$	Petigura et al. (2017)
Mass M_{\star} [M_{\odot}]	1.05 ± 0.04	Johnson et al. (2017)
Radius R_{\star} [R_{\odot}]	1.253 ± 0.051	Berger et al. (2018)
Age [Gyr]	4.7 ± 1.2	Johnson et al. (2017)
Projected rotation rate, $v_{\text{rot}} \sin i_{\star}$ [km s $^{-1}$]	2.8 ± 1.0	Petigura et al. (2017)
Rotation period P_{rot} [days]	12.89 ± 0.19	Angus et al. (2018)
<i>Planetary Parameters</i>		
Planet-to-star radius ratio, R_{p}/R_{\star}	0.0063 ± 0.0003	This work
Radius R_{p} [R_{\oplus}]	0.86 ± 0.04	This work
Time of inferior conjunction [BJD]	2454965.6804 ± 0.0003	This work
Orbital period P_{orb} [days]	2.465024 ± 0.000005	Thompson et al. (2018)
Orbital inclination i_{orb} [deg]	81.85 ± 0.10	This work

plays a key role in the asteroseismic analysis. Section 4 describes the asteroseismic analysis, and resolves the prior discrepancy by identifying a problem with the analysis by Campante et al. (2016). Section 5 shows that our asteroseismic estimate of i_{\star} agrees with the constraint that is obtained by combining measurements of the stellar radius, rotation period, and sky-projected rotation velocity. Our findings and some implications are summarized in Section 6. Just for definiteness, the present paper refers to those systems as *misaligned* if either λ (sky-projected spin-orbit angle) or $90^{\circ} - i_{\star}$ (a proxy for the stellar obliquity in transiting planetary systems) exceeds 30° in 95% confidence.

2. TRANSIT MODELING

The orbital inclination, i_{orb} , of a transiting planet is always close to 90° . For a precise measurement, we modeled the *Kepler* transit light curve. We downloaded the short-cadence, pre-search data conditioning (PDC) light curves from the Mikulski Archive for Space Telescopes. The data surrounding each transit were fitted with a standard model for the loss of light (Mandel & Agol 2002), assuming the orbit to be circular and accounting for stellar variability with a locally quadratic function of time. After dividing through by the best-fitting quadratic functions, the transit data were phase-folded and averaged, giving a mean light curve with a higher signal-to-noise ratio (Figure 1).

This light curve was then fitted to obtain our final estimates for the transit parameters (Table 1). Uniform priors were adopted for the logarithm of the planet-to-star radius ratio (R_{p}/R_{\star}), the cosine of the orbital inclination ($\cos i_{\text{orb}}$), the normaliza-

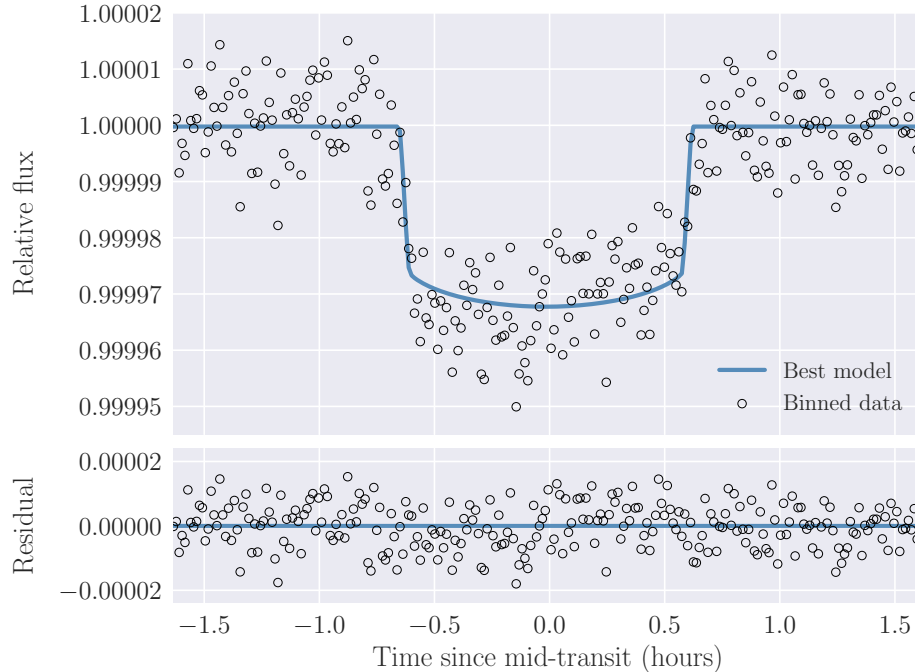


Figure 1. Phase-folded transit light curve of Kepler-408b. *Upper panel* — Binned data (open circles) with the best-fitting model (thick line). *Lower panel* — Residuals between the data and the best-fitting model.

tion of the light curve, the two coefficients of the quadratic limb-darkening profile, and the logarithm of a noise term to account for the scatter of the residuals between the data and the model. A Gaussian prior was adopted for the mean stellar density ($\rho_{\star} = 0.816 \pm 0.025 \text{ g cm}^{-3}$) based on the previous asteroseismic analysis of Kamiaka et al. (2018). The posterior distributions for the model parameters were obtained with a nested sampling code (Feroz et al. 2009). The result for the orbital inclination was $i_{\text{orb}} = 81.85 \pm 0.10$ degrees.

In the present analysis, we adopted the circular model because the time-scale for tidal orbital circularization is likely short for the 2.5-day orbit. We also checked that the model with non-zero eccentricity does not significantly improve the fit. This is in agreement with the analysis of Van Eylen et al. (2018), who found that the eccentricity was consistent with zero within 95% confidence.

3. STELLAR ROTATION PERIOD FROM PHOTOMETRIC VARIABILITY

The *Kepler* photometric time series exhibits quasi-periodic modulation that is presumably due to the rotation of surface inhomogeneities across the star’s visible hemisphere. By computing the autocorrelation function, McQuillan et al. (2013) determined the photometric rotation period to be 12.44 ± 0.17 days. Angus et al. (2018) reported a value of 12.89 ± 0.19 days by modeling the *Kepler* data as a Gaussian process with a quasi-periodic covariance kernel function.

To perform an independent check on the determination of the stellar rotation period, we analyzed the *Kepler* data outside of transits. We normalized the data from each

quarter by setting the median flux equal to unity. A Lomb-Scargle periodogram of the resulting time series has its most prominent peak at 12.96 ± 0.07 days, and the autocorrelation function shows a series of peaks spaced by 12.94 ± 0.22 days (Figure 2). Previous experience has shown that the strongest photometric periodicity sometimes occurs at harmonics of the true rotation period, presumably because there are several active regions on the star.

In the present case, visual inspection of the light curve confirms that the true period is close to 12.9 days. We were able to identify several time intervals in which a complex pattern of variations repeats nearly exactly after 12.9 days (Figure 3), which would be an unlikely coincidence if the true period were different. We highlighted part of the lightcurves in Figure 3 so as to clarify the periodicity, but it should be regarded as a *sanity check* on the more objective measures with no claim to be objective or complete. For a more systematic comparison between asteroseismic and photometric estimates of stellar rotation periods for other stars, see Suto et al. (2019).

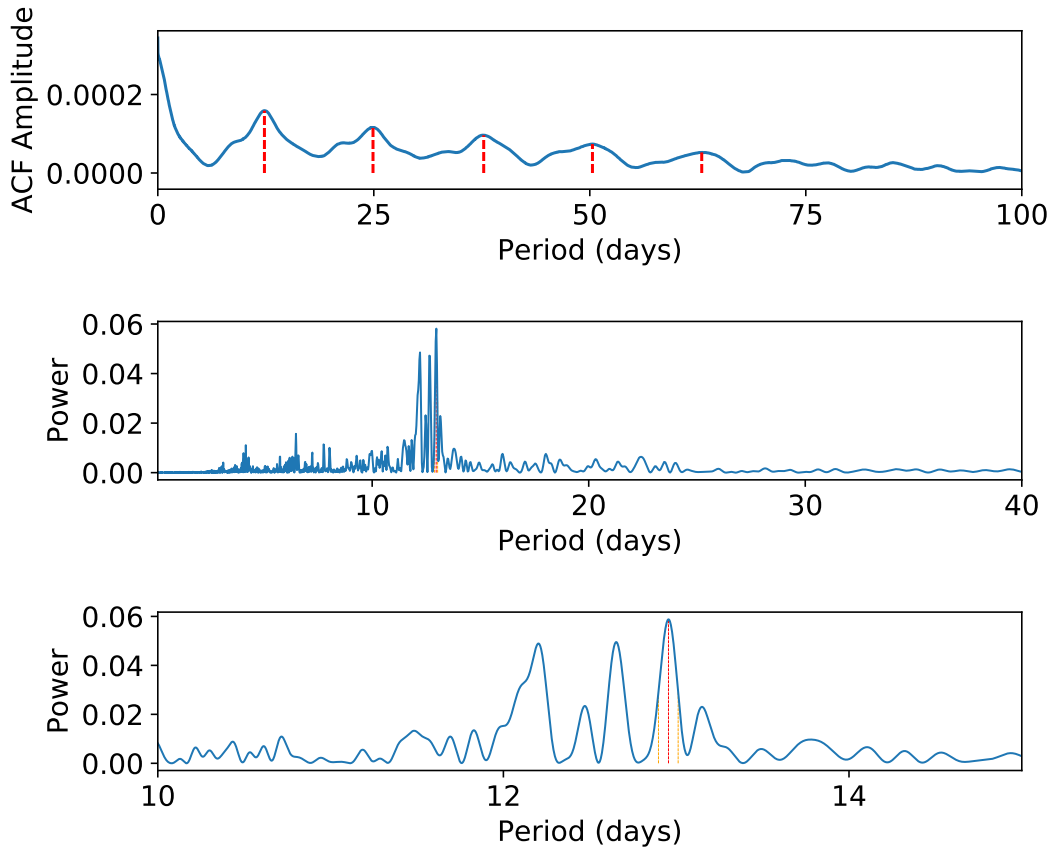


Figure 2. Estimates of the stellar rotation period from the photometric time series. *Top:* Auto-correlation function. The red dashed lines indicate the locations of several peaks. *Middle:* The Lomb-Scargle periodogram. The location of the most significant peak is marked with a red dashed line, and the 1σ uncertainty interval is plotted with orange dashed lines. *Bottom:* Close-up of the Lomb-Scargle periodogram around the most significant peak.

In what follows, we adopt the value $P_{\text{rot}} = 12.89 \pm 0.19$ days based on the work of [Angus et al. \(2018\)](#), since their analysis appears to be the most rigorous with regard to the quoted uncertainty. The reciprocal of the rotation period, which is most relevant to the asteroseismic analysis, is $1/P_{\text{rot}} = 0.898 \pm 0.013 \mu\text{Hz}$.

4. ASTEROSEISMIC ANALYSIS

4.1. *Brief description of the method*

The star’s pressure-mode oscillations (p modes) are manifest in the *Kepler* data as quasi-periodic variations in stellar brightness with amplitudes of a few parts per million (ppm) and frequencies on the order of $2000 \mu\text{Hz}$ (periods ~ 10 min). The modes can be classified with three integers: the radial order $n(\geq 1)$, which depends

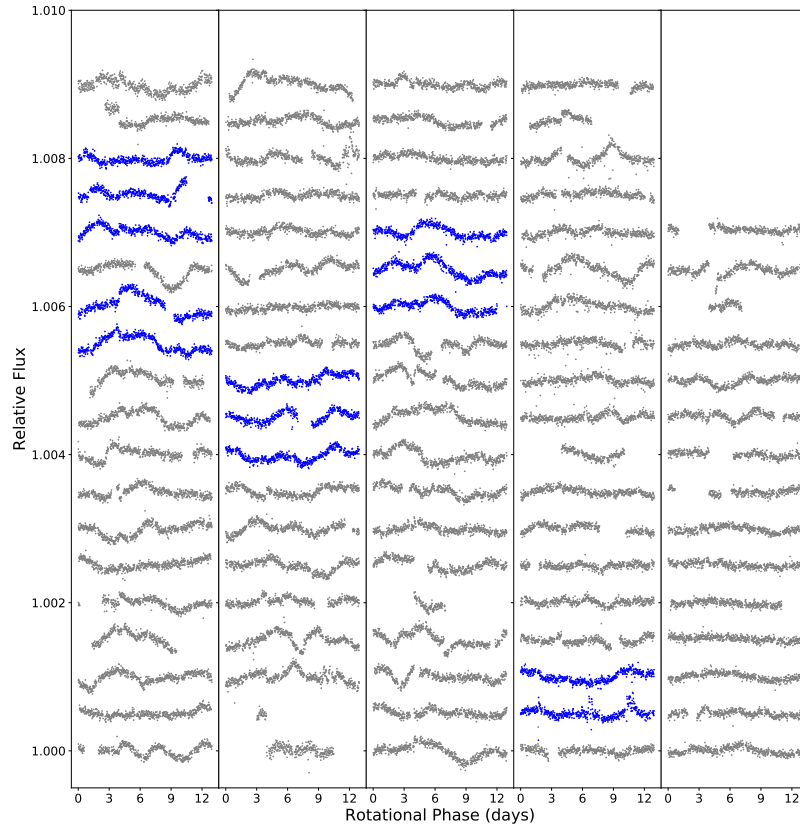


Figure 3. Confirmation of the rotation period through visual inspection. Shown is the entire *Kepler* light curve, folded with the candidate 12.94-day period. Vertical offsets have been applied to each cycle of data in order to separate them; they are organized like the lines of text on a page. Highlighted in blue are several occasions where the pattern of flux variation is similar from one rotation to the next. This would be unlikely if the rotation period had been misidentified.

on the radial dependence of the oscillatory pattern; the angular degree $\ell (\geq 0)$, which specifies the variation with the polar angle; and the azimuthal order $m (= -\ell \dots 0 \dots \ell)$, which specifies the variation with the azimuthal angle. For a non-rotating star, all the modes with the same n and ℓ would have the same frequency, regardless of m . Rotation breaks this degeneracy, producing small frequency shifts:

$$\nu_{n,\ell,m} = \nu_{n,\ell} + m\delta\nu_\star \approx \left(n + \frac{\ell}{2} + \varepsilon_{n,\ell}\right) \Delta\nu + m\delta\nu_\star, \quad (1)$$

where $\Delta\nu$ is the “large separation” (the spacing between consecutive radial modes), $\varepsilon_{n,\ell}$ is a small correction of order unity (Tassoul 1980, 1990; Mosser et al. 2013), and the rotational splitting $\delta\nu_\star$ is approximately the reciprocal of the stellar rotation period (Appourchaux et al. 2008).

Because the shifts are small ($\delta\nu_\star \sim 1 \mu\text{Hz}$), all the modes within a multiplet are expected to have the same intrinsic amplitude. However, the height of each peak in the observed power spectrum is also proportional to a factor $\mathcal{E}_{\ell,m}$ depending on the rotational inclination i_\star as shown in equations (2) and (4) below. This is because the peak heights are based on the average intensity of the mode pattern across the visible hemisphere, and the modes have different symmetries with respect to the rotation axis.

4.2. Power spectrum modeling

We downloaded the Kepler-408 power spectrum from the Kepler Asteroseismic Science Operations Center database. We modeled the power spectrum as

$$P(\nu) = \sum_{n=n_{\min}}^{n_{\max}} \sum_{\ell=0}^{\ell_{\max}} \sum_{m=-\ell}^{+\ell} \frac{H_{n,\ell} \mathcal{E}_{\ell,m}(i_\star)}{1 + \left(\frac{\nu - \nu_{n,\ell,m}}{\Gamma_{n,\ell,m}/2}\right)^2} + N(\nu), \quad (2)$$

where $H_{n,\ell}$ is the intrinsic mode amplitude, $\mathcal{E}_{\ell,m}(i_\star)$ is the mode visibility (see equation 4), $\nu_{n,\ell,m}$ is the line center, $\Gamma_{n,\ell,m}$ is the line width, and $N(\nu)$ is the noise background. The background was modeled as

$$N(\nu) = \frac{A_1}{1 + (\tau_1\nu)^{p_1}} + \frac{A_2}{1 + (\tau_2\nu)^{p_2}} + N_0, \quad (3)$$

where N_0 is a constant (white noise), and A_i , τ_i , and p_i ($i = 1, 2$) are the height, characteristic time scale, and slope of a Harvey-like profile. Further details are given by Kamiaka et al. (2018).

The most readily observed multiplets are the dipole ($\ell = 1$) and quadrupole ($\ell = 2$) modes, for which

$$\begin{aligned} \mathcal{E}_{1,0} &= \cos^2 i_\star, & \mathcal{E}_{1,\pm 1} &= \frac{1}{2} \sin^2 i_\star, \\ \mathcal{E}_{2,0} &= \frac{1}{4} (3 \cos^2 i_\star - 1)^2, & \mathcal{E}_{2,\pm 1} &= \frac{3}{8} \sin^2 2i_\star, & \mathcal{E}_{2,\pm 2} &= \frac{3}{8} \sin^4 i_\star. \end{aligned} \quad (4)$$

For a star with $i_\star = 90^\circ$, the central peak ($m = 0$) is missing, while for $i_\star = 0^\circ$, only the central peak is visible (e.g., [Gizon & Solanki 2003](#)).

The power spectrum was analyzed using a Markov Chain Monte Carlo algorithm based on a Metropolis-Hasting scheme, with parallel tempering. We divided the analysis into three steps: the burn-in phase, training phase, and acquire phase. The burn-in phase (40,000 samples) ensures that we reach the region of interest in the parameter space. The training phase (700,000 samples) employs an adaptive algorithm to optimize the covariance matrix of the Gaussian proposal probability density function to achieve the ideal acceptance rate of 23.4% ([Atchade 2006](#)). During the acquire phase (10^6 samples), the optimal covariance matrix is used to sample the posterior distribution. Convergence of the posterior distribution is confirmed through the Heidelberg-Welch and Geweke tests.

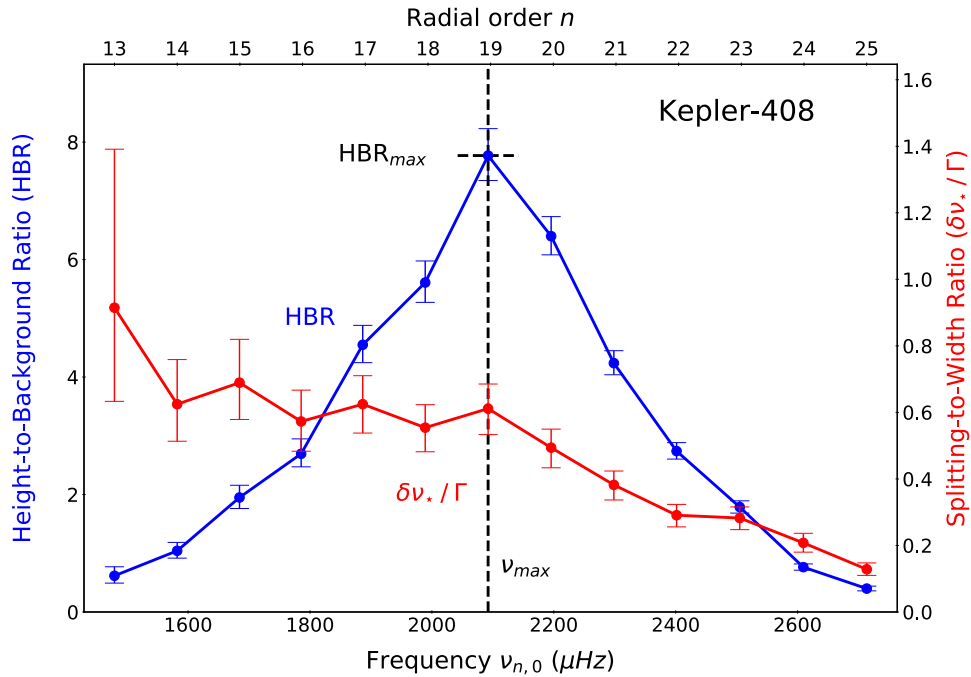


Figure 4. Key parameters for the reliable inference of rotational inclination. The blue curve shows the height-to-background ratio (HBR) for the $\ell = 0$ modes. The red curve shows the ratio between the frequency splitting $\delta\nu_\star$ and the line width Γ for the $\ell = 0$ modes.

Because of the large number of free parameters, we fitted the spectrum in two steps. First, we concentrated on fitting the background, using a single Gaussian function to model the envelope of excess power from the oscillation modes. The results for the background model were then used as priors when fitting for the parameters of the oscillation modes. Figure 4 plots the height-to-background ratio (HBR) and the splitting-to-width ratio ($\delta\nu_\star/\Gamma$) as a function of mode frequency $\nu_{n,l=0}$, showing that HBR takes the maximum value HBR_{max} at ν_{max} . [Kamiaka et al. \(2018\)](#) found that

reliable inference of i_\star practically requires at least $\text{HBR}_{\text{max}} \gtrsim 1$ and $\delta\nu_\star/\Gamma(\nu_{\text{max}}) \gtrsim 1/2$. As indicated by the dashed line in Figure 4, their criteria are satisfied for Kepler-408.

We inspected each line-profile visually so as to avoid too noisy modes, and selected the radial orders of $13 \leq n \leq 25$ for $\ell = 0$ and 1, and $12 \leq n \leq 24$ for $\ell = 2$, respectively, for the analysis. Figures 5 and 6 give the mode profiles for $\ell = 1$ ($13 \leq n \leq 24$) and for $\ell = 2$ ($12 \leq n \leq 23$), respectively. In those panels our best-fits of $i_\star = 42^{+5}_{-4}$ degrees and $\delta\nu_\star = 0.99 \pm 0.10 \mu\text{Hz}$ are plotted in solid green lines (see Figure 7 below).

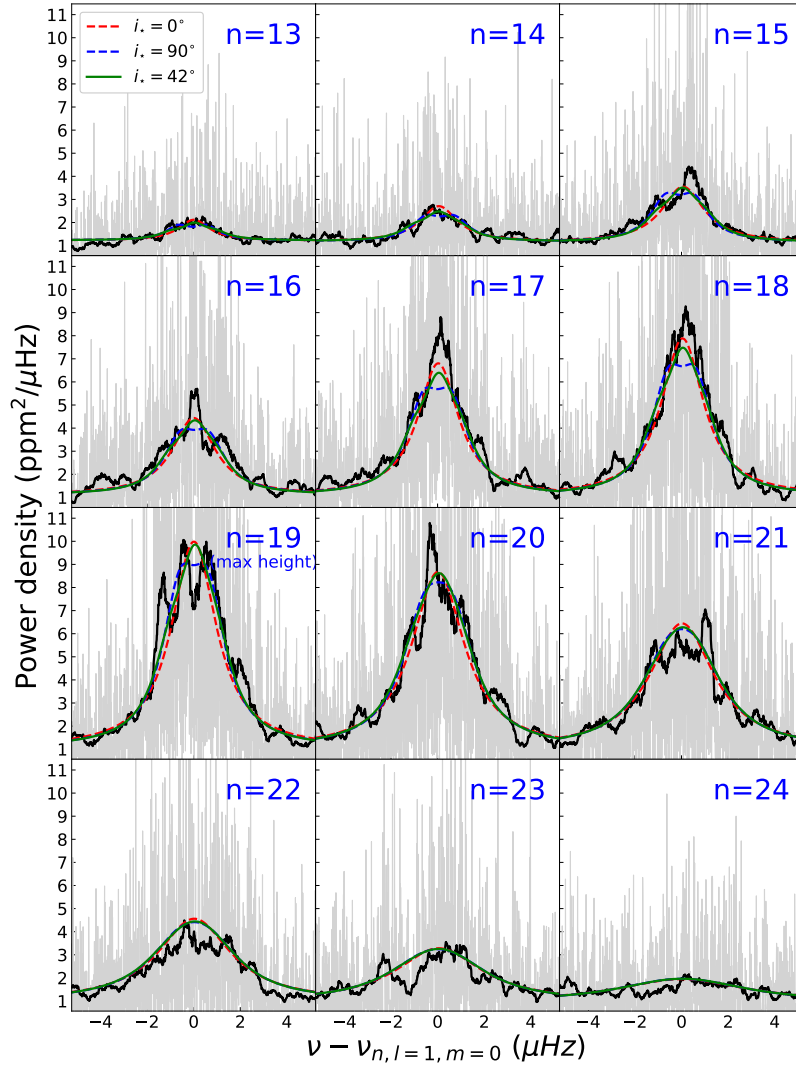


Figure 5. Individual profiles for dipole modes ($\ell = 1$) for the radial orders from $n = 13$ to 24. In each panel, the gray and black lines represent the unsmoothed and smoothed (with a boxcar kernel of width $0.5 \mu\text{Hz}$), respectively. The fitting results assuming $i_\star = 0^\circ$ and 90° are plotted in red and blue, respectively, while our best-fit model with treating i_\star as a free parameter is plotted in green ($i_\star = 42^\circ$).

4.3. Checks for consistency and robustness

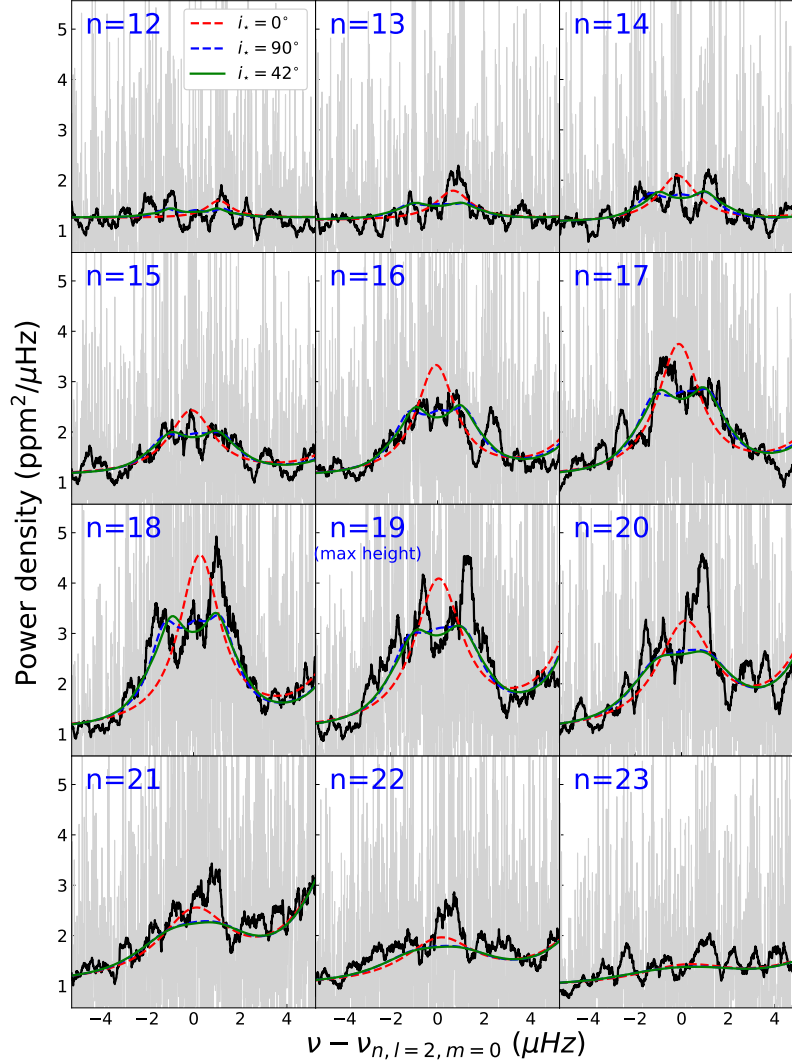


Figure 6. Same as Figure 5, but for quadrupole modes ($\ell = 2$) from $n = 12$ to 23.

The measured splitting is in agreement with the value of $1/P_{\text{rot}} = 0.898 \pm 0.013 \mu\text{Hz}$ based on the photometric rotation period, thereby providing a successful consistency check. We also tried using the photometric rotation period as a prior constraint on the asteroseismic analysis, which sharpened the constraint on the stellar inclination angle to 45.9 ± 2.1 degrees (see the blue curves in Figure 7).

To allow for a visual inspection, Figure 8 displays the average $\ell = 1$ and $\ell = 2$ profiles, based on the combination of the data from 13 different radial orders. The profile of the average $\ell = 1$ multiplet (the top panel) is centrally peaked, demonstrating the visibility of the $m = 0$ mode, and ruling out an inclination angle near 90° . The signal-to-noise ratio and frequency resolution are high enough that the absence of the $m = 0$ mode would have led to a flat-topped appearance, from the combination of the marginally resolved $m = +1$ and -1 modes. On the other hand, the profile of

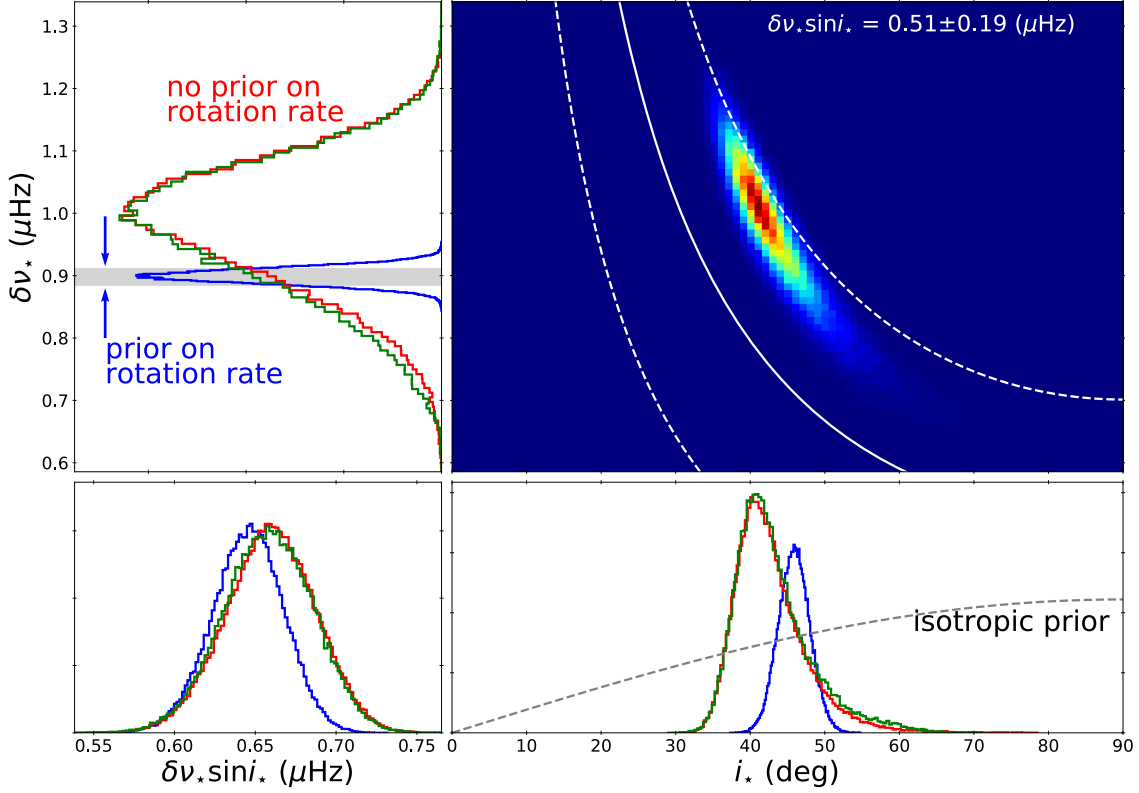


Figure 7. Constraints on rotational inclination and frequency splitting. Shown is the posterior probability density (PPD) in the space of i_* and $\delta\nu_*$, marginalized over all other parameters. The one-dimensional marginalized densities are also shown to the left and below the axes. The panel in the bottom left is the PPD of $\delta\nu_* \sin i_*$, which is more tightly constrained than either $\delta\nu_*$ or i_* . The red and blue histograms are the PPDs without and with a prior constraint of $\delta\nu_* = 0.898 \pm 0.013 \mu\text{Hz}$ based on the measured rotation period. The white lines identify the region where $\delta\nu_* \sin i_* = 0.51 \pm 0.19 \mu\text{Hz}$, the value that is independently determined from measurements of $v_{\text{rot}} \sin i_*$ and R_* (see Section 5). The bottom-right panel indicates the marginalized PPD for the stellar inclination i_* . The median and 68% (95%) credible interval are $i_* = 41.7^{+5.1}_{-3.5}$ ($i_* = 41.7^{+13.3}_{-6.4}$) based on asteroseismology alone. When the prior on rotation rate is applied, the results become $i_* = 45.8^{+2.1}_{-2.2}$ ($i_* = 45.8^{+4.4}_{-4.3}$). The result incorporating the apodization factor in our background noise model (green lines) is almost indistinguishable (see Section 4.4).

the $\ell = 2$ modes is not centrally peaked, ruling out inclinations near zero. Together, the appearance of the modes suggests an intermediate value of the inclination.

The bottom panel of Figure 8 shows that the $\ell = 2$ multiplet has an asymmetric appearance, with more power at frequencies above the line center than below. This is unexpected because the geometrical factors $\mathcal{E}_{\ell,m}$ do not depend on the sign of m . Figure 6 suggests that this asymmetry in power is mainly due to modes of high radial order ($n = 18$ to 21). Such high-order modes are more sensitive to the conditions near the stellar surface (e.g. Christensen-Dalsgaard & Thompson 1997; Kjeldsen et al. 2008; Ball & Gizon 2014; Sonoi et al. 2015). Thus, the observed asymmetry may arise from the (poorly understood) magnetic and non-adiabatic processes occurring near the surface. We performed the similar stacking analysis for several stars in Kamiaka et al.

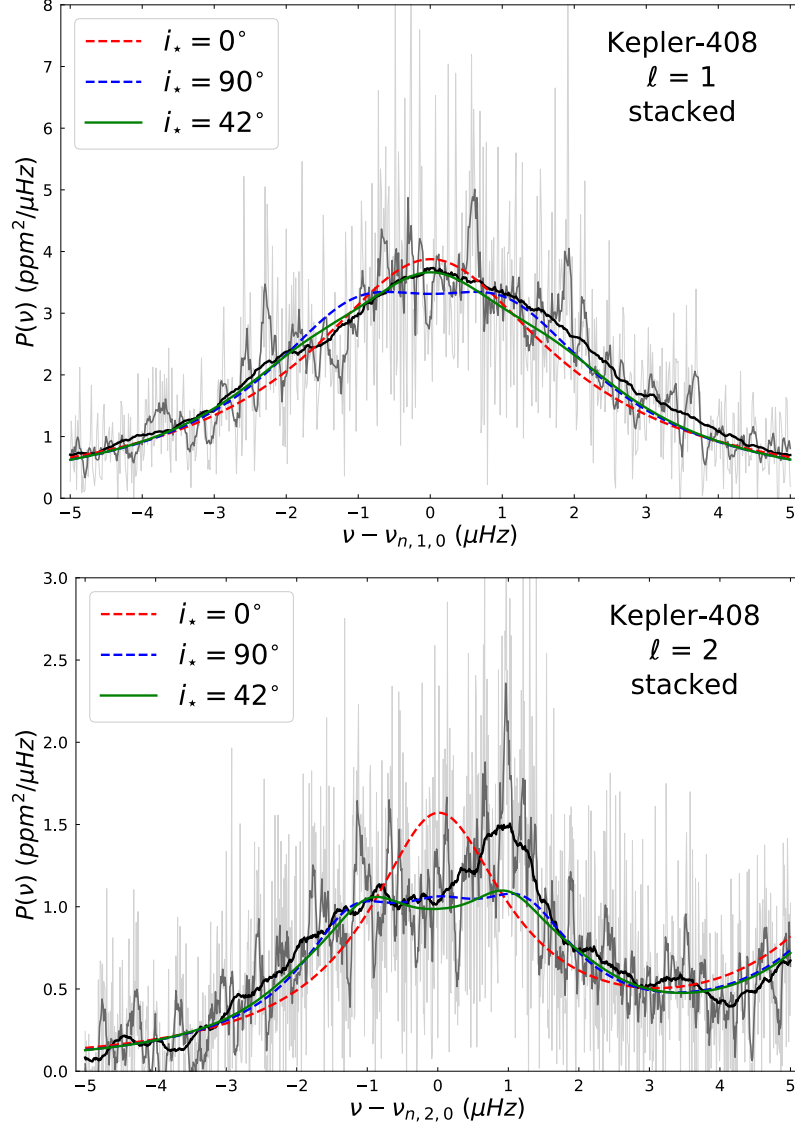


Figure 8. Average power spectra of rotationally split multiplets, for $\ell = 1$ (top) and $\ell = 2$ (bottom). The profiles of multiple modes have been stacked to improve the signal-to-noise ratio and allow for a visual inspection, although the quantitative fits were performed on the data without any averaging or stacking (see Figs. 5 and 6). For $\ell = 1$, the modes with $n = 13$ to 25 were included. For $\ell = 2$, the modes with $n = 12$ to 24 were included. The thin gray line shows the data without any smoothing, while the thick gray and black lines show the data after smoothing over 0.05 and 0.75 μHz in frequency, respectively. Each panel also shows three model curves that were optimized to fit the data. The red curve is based on a model assuming $i_* = 0^\circ$, the blue curve is for $i_* = 90^\circ$, and the green curve is for a model in which i_* is a free parameter. For the $\ell = 2$ modes, the gradual rise observed at the high-frequency end is from a neighboring radial mode ($\ell = 0$). The asymmetry in the line profile is not understood (see Section 4.3).

(2018), all of which do not exhibit any noticeable asymmetry. Thus the asymmetry seems fairly specific to Kepler-408. Because the reason for the asymmetry is not clear, we tried fitting only the $\ell = 1$ modes and found that a low inclination (and a high stellar obliquity) are still preferred as shown in Figure 9c below.

We repeated the fit after decreasing the amplitude of the (unsmoothed) data by 30% for $-\Gamma_{n,l=2,m=0}/2 < \nu - \nu_{n,l=2,m=1} < \Gamma_{n,l=2,m=0}/2$ for $18 \leq n \leq 21$, and found that $i_\star = 39_{-3}^{+4}$ degrees. Since fitting these simulated spectra did not lead to any systematic bias in the results for the inclination, the observed asymmetry for the $\ell = 2$ modes does not affect our conclusion that Kepler-408b has a significantly misaligned orbit.

As further tests of robustness, we repeated the analysis for 5 different choices of the set of radial orders and angular degrees to be fitted (see Figure 9). This led to larger uncertainties, and small systematic changes in the derived parameters. Fitting the $\ell = 1$ modes tends to give lower inclinations, while the $\ell = 2$ modes favor higher inclinations. Such complementary roles of $\ell = 1$ and $\ell = 2$ modes are very useful in constraining i_\star and $\delta\nu_\star$ reliably. While Kepler-408 is one of the stars with the clearest pulsation spectrum, its asteroseismic modeling is still subtle and careful individual tests are required for the reliable parameter extraction.

In all cases, though, the results are compatible with a large spin-orbit misalignment, and the splitting is compatible with the photometric rotation period, implying that our asteroseismic inference for the Kepler-408 system is robust.

4.4. Comparison with previous results

In reality, our results do not agree with those of [Campante et al. \(2016\)](#), who found $i_\star > 54^\circ$ within 1σ confidence (we note, however, that their 95.4% constraint is $i_\star > 36.5^\circ$). In attempting to understand the reason for the discrepancy, we realized that we use an unweighted power spectrum (Lomb-Scargle periodogram), while [Campante et al. \(2016\)](#) computed it using a weighted least-square-fitting method. Thus we repeated our analysis using their spectrum, and obtained almost the same inclination angle, implying that the difference of the spectra is not a major reason for the discrepancy. We also noticed that their best fitting model gave $\delta\nu_\star = 0.50_{-0.04}^{+0.20} \mu\text{Hz}$, which is inconsistent with the photometrically measured rotation period. Another difference is related to the chosen model for the background noise in the power spectrum. For the sake of uniformity, [Campante et al. \(2016\)](#) adopted the same model for all 25 systems of their analysis. Their model was parameterized as:

$$B(\nu) = B_0 + \left[\frac{B_1}{1 + (2\pi\nu\tau_1)^a} + \frac{B_2}{\nu^2} \right] \text{sinc}^2 \left(\frac{\pi\nu}{2\nu_0} \right), \quad (5)$$

where $\nu_0 = 8496.6 \mu\text{Hz}$ is the Nyquist frequency.

While equation (5) works reasonably well in general, the residuals from the best-fit of their noise model (right panels of Figure 10) shows that it poorly fits the low-frequency part of the noise background of Kepler-408; There is a systematic departure from the zero baseline of up to 10% in the vicinity of the low-frequency modes, suggesting that their noise background fit is not satisfactory. In contrast, our background model, equation (3), fits much better, as illustrated in the left panels of Figure 10. More specifically, our best-fit model based on our power spectrum with the background model (3) is preferred over that based on the Campante et al. power spectrum with

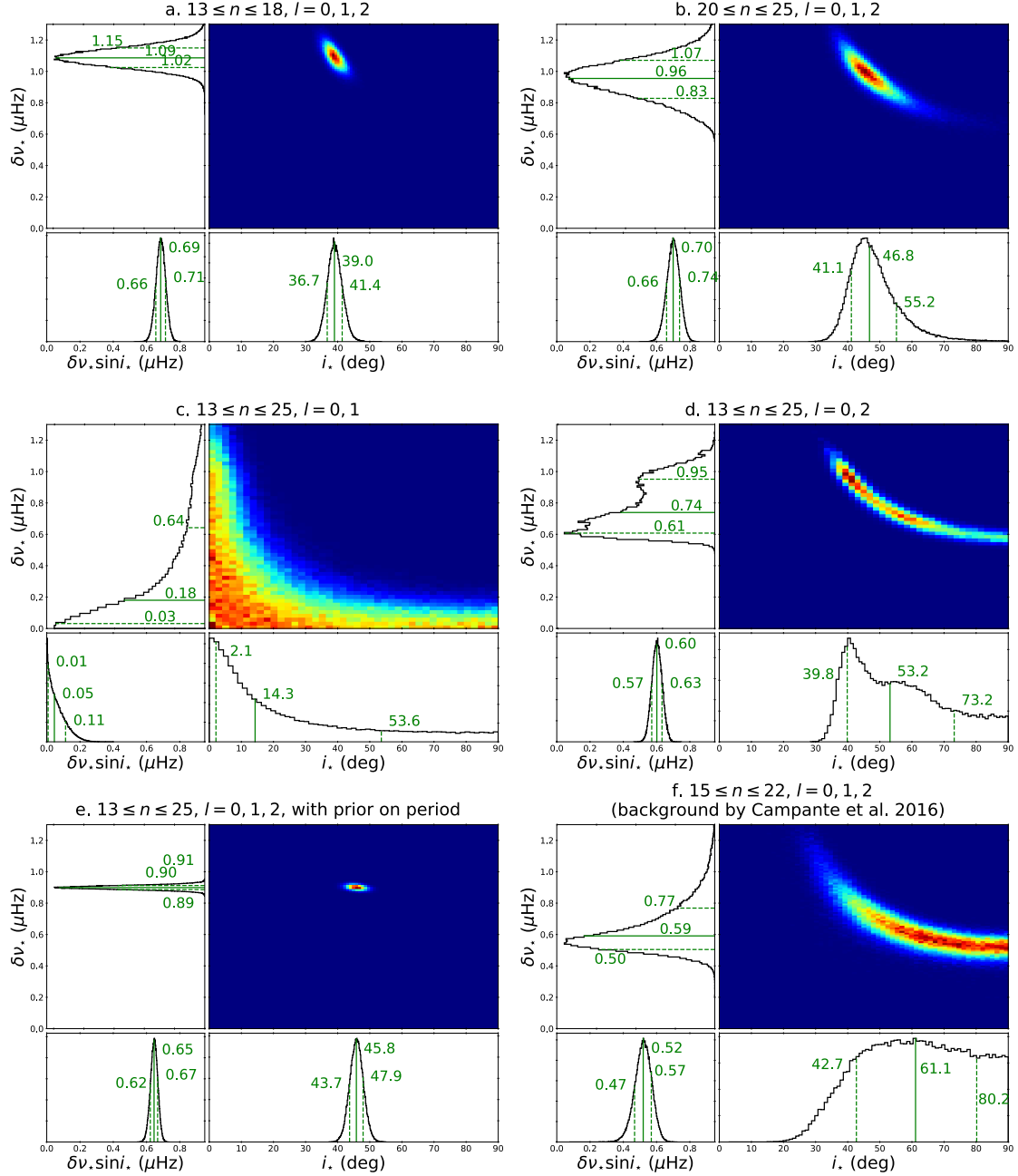


Figure 9. Constraints on i_* and $\delta\nu_*$, as in Fig. 7, after making variations in the analysis procedure. *a*: Fitting only the lower radial orders ($13 \leq n \leq 18$) and $\ell = 0, 1, 2$. *b*: Fitting only the higher radial orders ($20 \leq n \leq 25$) and $\ell = 0, 1, 2$. *c*: Fitting only the radial and dipole modes ($\ell = 0, 1$) of all orders. *d*: Fitting only the radial and quadrupole modes ($\ell = 0, 2$) of all orders. *e*: Fitting $\ell = 0, 1, 2$ of all orders, with a Gaussian prior of $\delta\nu_* = 0.898 \pm 0.013 \mu\text{Hz}$ based on the measured rotation period (Angus et al. 2018). *f*: Fitting all orders and modes, after replacing our model for the noise background with the (unsatisfactory) model of Campante et al. (2016). The green solid and dashed lines in the histograms indicate the median and 1σ credible regions.

equation (5) by an “odds ratio” significantly larger than 100. The odds ratio is the ratio of the two integrated likelihoods; see section 12.7 of Gregory (2005) for details.

According to the [Jeffreys \(1961\)](#) classification, this is a decisive evidence in favor of our background noise model.

Incidentally equation (3) does not include the apodization correction factor $\text{sinc}^2(\pi\nu/2\nu_0)$ unlike equation (5). This could affect the estimate of i_* . We assessed this possibility by applying the correction for the first two terms in equation (3) as in [Davies et al. \(2016\)](#), and found that the resulting fit yields $i_* = 41.9^{+5.7}_{-3.6}$ degrees (see green histogram in Figure 7). Thus we confirm that the apodization factor does not change our conclusion.

When we replaced our model for the background with that of equation (5), we were able to reproduce the result of $i_* > 54^\circ$ reported by [Campante et al. \(2016\)](#). Evidently, it is essential to perform a careful subtraction of the low-frequency noise for each system, to obtain an unbiased estimate of i_* from asteroseismic analysis. [Appourchaux, T. et al. \(2012\)](#) have studied the systematic errors in measurements of seismic parameters caused by inaccuracies in the model for background noise. Although they did not examine the implications for inference of the inclination angle, they did note that inaccuracies can greatly impact the inferred mode heights and linewidths, which in turn may bias the measurement of the rotational splitting and inclination. Our work demonstrates that this is indeed the case: systematic errors in the background model can severely bias the measured inclination.

As an additional test, we tried replacing the background model with a simple quadratic function of frequency. By restricting the frequency range to the limited interval spanned by the oscillation modes (1300–2900 μHz), we found that the quadratic function also gives a good fit. The results for the inclination were the same as in our original analysis ($i_* = 42^{+5}_{-4}$ degrees), confirming that the exact functional form of the background model does not matter, as long as it fits reasonably well.

5. PROJECTED ROTATION RATE

There is also evidence independent of asteroseismology that the rotational inclination is in the neighborhood of 45° , based on the measured values of the stellar radius, rotation period, and sky-projected rotation velocity (Table 1). The stellar radius (R_*) was determined by combining the observed geometric parallax, apparent K magnitude, and spectroscopic effective temperature ([Berger et al. 2018](#)). The rotation period (P_{rot}) was determined from the *Kepler* photometry, as noted above. The combination of these quantities implies $v_{\text{rot}} = 2\pi R_*/P_{\text{rot}} = 4.92 \pm 0.21 \text{ km s}^{-1}$. Meanwhile, the sky-projected rotation velocity ($v_{\text{rot}} \sin i_*$) was found to be $2.8 \pm 1.0 \text{ km s}^{-1}$ by modeling the Doppler-rotational contribution to the observed spectral line broadening ([Petigura et al. 2017](#)).

Together, these data can be used to place constraints on $\sin i_*$. To obtain the likelihood function for $\sin i_*$, we integrated $p_1(v_{\text{rot}}) \cdot p_2(v_{\text{rot}} \sin i_*)$ over v_{rot} , where p_1 and p_2 are Gaussian functions representing the constraints $v_{\text{rot}} = 4.92 \pm 0.21 \text{ km s}^{-1}$ and

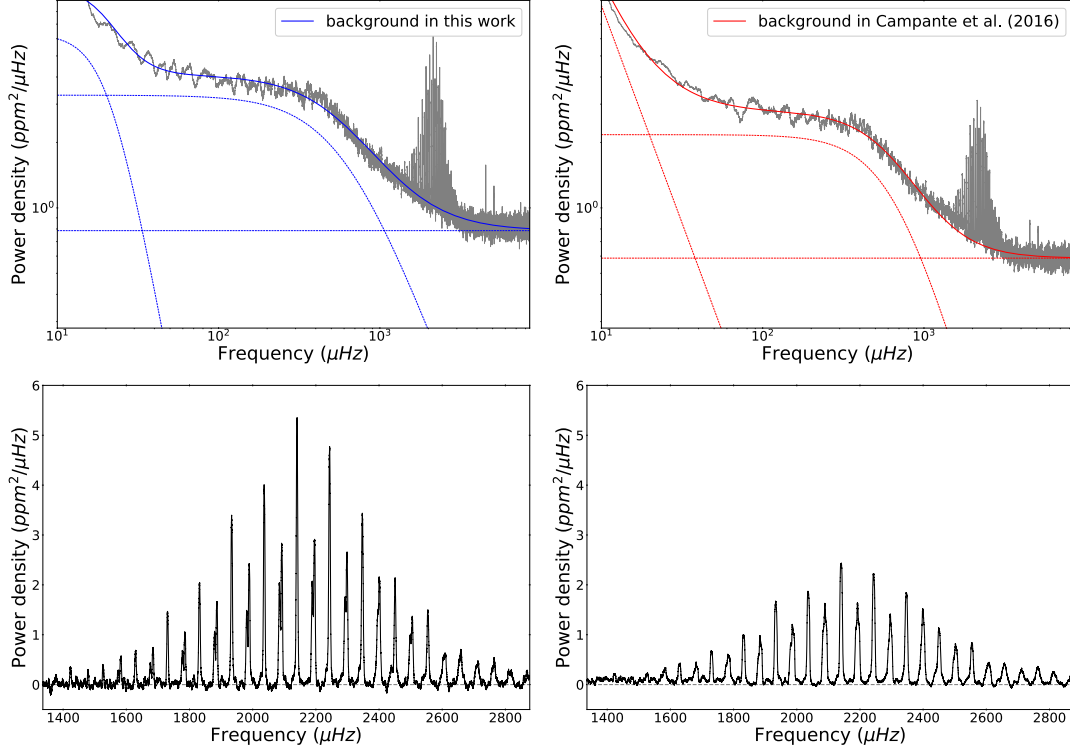


Figure 10. Models of the noise background. *Top panels.* — The entire power spectrum of Kepler-408, along with the best-fitting model and its three separate components. The left panel shows the spectrum and model used in our analysis. The right panel shows those used in [Campante et al. \(2016\)](#), which does not fit well the lower envelope of the power spectrum in the vicinity of the oscillation modes. *Bottom panels.* — Close-up of the oscillation modes, after subtracting the best-fitting model for the background.

$v_{\text{rot}} \sin i_{\star} = 2.8 \pm 1.0 \text{ km s}^{-1}$. The result is $\sin i_{\star} = 0.70 \pm 0.21$, or $i_{\star} = 44^{+20}_{-15}$ degrees, which is consistent with our asteroseismic result.

As another consistency check, we can combine the spectroscopically determined $v_{\text{rot}} \sin i_{\star}$ and R_{\star} to give $\delta\nu_{\star} \sin i_{\star} = 0.51 \pm 0.19 \text{ } \mu\text{Hz}$. The white lines in Figure 7 show the region that is defined by this constraint, which is independent of the asteroseismic analysis. The results are again consistent to within $1\text{-}\sigma$.

6. SUMMARY

By modeling the power spectrum of p modes, we found the stellar inclination to be $i_{\star} = 41.7^{+5.1}_{-3.5}$ ($i_{\star} = 41.7^{+13.3}_{-6.4}$) degrees with 68% (95%) credible interval (Section 3). [Nielsen et al. \(2017\)](#) and [Kamiaka et al. \(2018\)](#) previously reported a similar result for Kepler-408, but did not remark on the conflict with the analysis of [Campante et al. \(2016\)](#), nor did they appreciate the importance of this system for understanding the origin of the spin-orbit misalignment (described below). The more thorough analysis in the present paper has resolved the conflict, by examining the individual and stacked line-profiles for different modes, comparing the best-fit with and without the photometric rotation period constraint, and exploring different possibilities for the background model. This experience with Kepler-408 and the methodology pre-

sented in this paper should allow for more robust determinations of i_* in the future, through the precise and accurate combination of asteroseismology, photometry and spectroscopy.

As for the inclination of the orbital axis, by fitting the *Kepler* light curve we found $i_{\text{orb}} = 81.85 \pm 0.10$ degrees (Section 2). Knowledge of both the rotational and orbital inclinations is not enough to determine the stellar obliquity, because both measurements are subject to the usual degeneracy $i \leftrightarrow 180^\circ - i$, and because we do not know the position angle on the sky between the two axes. Nevertheless we may set a lower limit on the stellar obliquity of $|i_{\text{orb}} - i_*| = 40 \pm 5$ (deg).

Of all the planets known to have a spin-orbit misalignment, Kepler-408b is the smallest by a factor of six, as illustrated in Figures 11 and 12. As described earlier, we classify systems as *misaligned* in those plots, if either their sky-projected spin-orbit angle λ or a proxy for the stellar obliquity in transiting systems, $90^\circ - i_*$, exceeds 30° in 95% confidence. The strong selection bias for the RM measurement towards larger planets and shorter orbital periods is clearly illustrated in the upper and lower panels of Figures 12, in contrast to the homogeneous selection for asteroseismic targets.

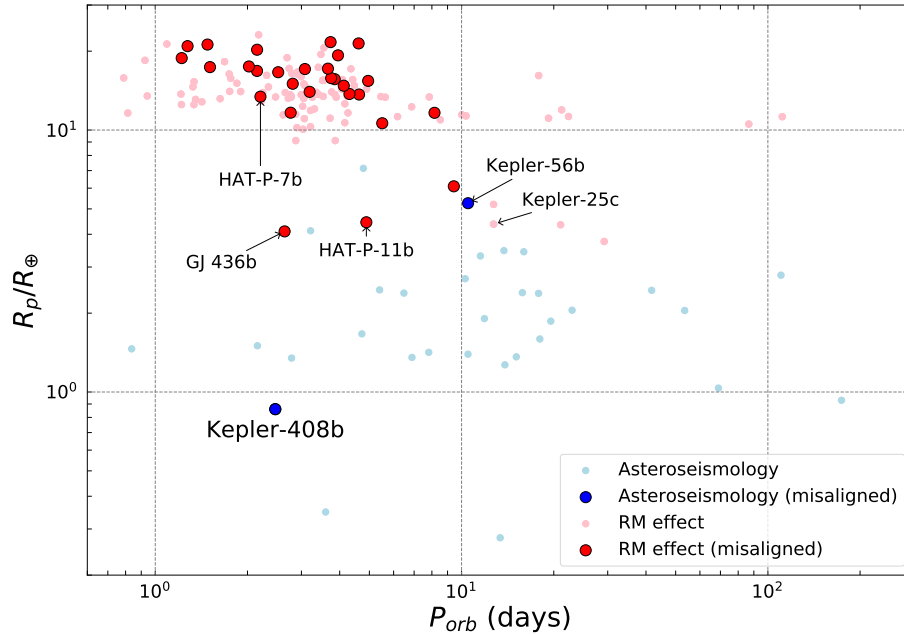


Figure 11. Sizes and orbital periods of planets for which the stellar obliquity has been constrained, based on the Rossiter-McLaughlin effect (red) and asteroseismology (blue). Misaligned planets (with their 2σ lower limit of either λ or $90^\circ - i_*$ exceeding 30°) are marked in bold symbols. Based on the compilation of Southworth (2011) and our measurement (Kamiaka et al. 2018).

Those figures also identify other systems of particular interest. Kepler-56 is an obliquely rotating star ($i_* \sim 45^\circ$) hosting two transiting planets (Huber et al. 2013). HAT-P-7 and Kepler-25 are the only known systems for which both Rossiter-McLaughlin and asteroseismic measurements have been successful (Benomar et al.

2014; Lund et al. 2014). HAT-P-11b and GJ 436b are the smallest planets previously known to be misaligned (Winn et al. 2010b; Yee et al. 2018; Bourrier et al. 2018).

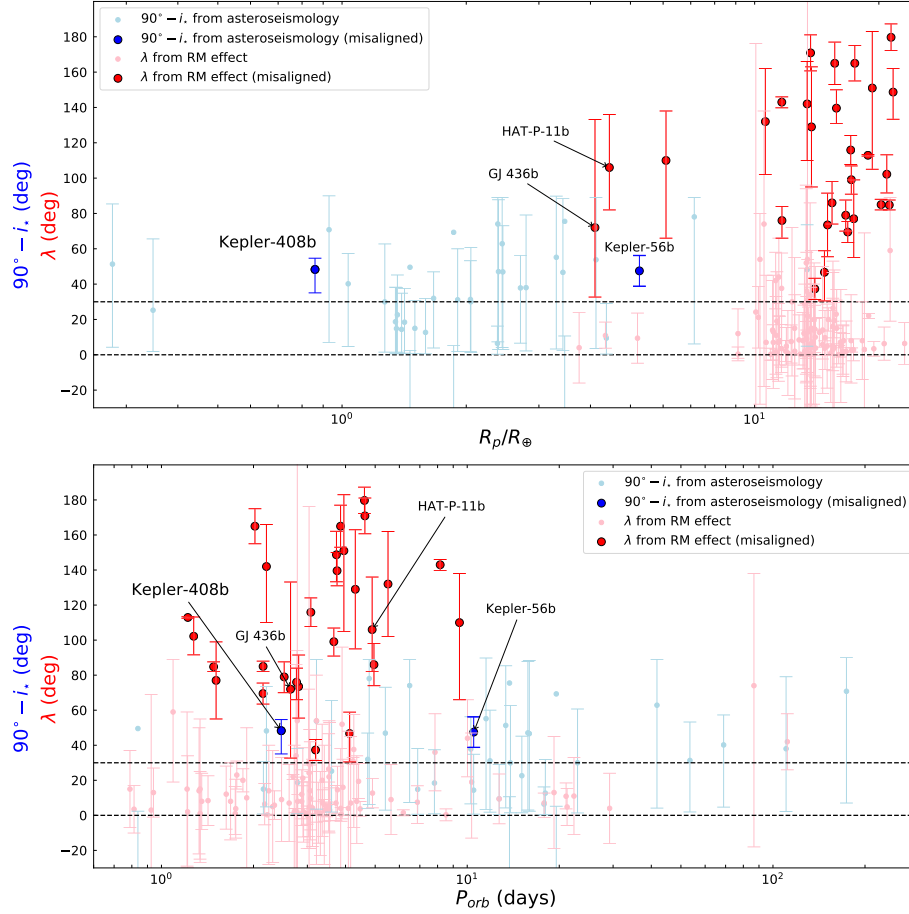


Figure 12. Observed spin-orbit angles for transiting exoplanets as a function of planetary radius and orbital period. Red symbols are for determinations of the position angle λ based on the Rossiter-McLaughlin effect (Southworth 2011). Blue symbols are for determinations of inclination based on asteroseismology (Huber et al. 2013; Campante et al. 2016; Kamiaka et al. 2018). For systems with more than one transiting planet, only the result for the innermost planet is plotted, with the sole exception of Kepler-25c. The plotted error bars correspond to 2σ (95%) confidence limits, and misaligned planets (with their 2σ lower limit of either λ or $90^\circ - i_*$ exceeding 30°) are marked in bold symbols. The horizontal dashed lines indicate 30° (our misalignment threshold) and 0° . Based on the compilation of Southworth (2011) and our measurement (Kamiaka et al. 2018).

Kepler-408 provides a clue about the origin of misalignments in general. Stars and their planets are thought to form in a well-aligned state. This is because the star and the protoplanetary disk inherit the same direction of angular momentum from an initial clump of gas that contracts under its own gravity. The observation of a large obliquity is an indication that something torqued the system out of alignment. The circumstances and the timing of the torque are unknown. Since all the previous cases of large obliquities involved planets larger than Neptune, some of the proposed theories have focused on giant planets. The data have often been regarded as evidence

that the formation of close-orbiting giant planets, including hot Jupiters, involves processes that tilt the planet’s orbit (Winn et al. 2010a; Triaud et al. 2010).

The case of Kepler-408 shows that orbit-tilting processes are not specific to giant planets, and must occur at least occasionally for “hot Earths.” In a recently proposed theory for the formation of very short-period terrestrial planets (Petrovich et al. 2018), an inner planet’s orbital angular momentum is reduced through chaotic long-term interactions with more distant planets, leading to spin-orbit misalignments of 10° – 50° , as observed here. Another theory involves a secular resonance with a more distant giant planet (Hansen & Zink 2015), although in the case of Kepler-408, no additional transiting planets are known. The existing Doppler data do not show any signals exceeding 4 m s^{-1} on timescales less than a year (Marcy et al. 2014). Other possibilities are that stars and their protoplanetary disks are occasionally misaligned due to torques from neighboring stars (Batygin 2012) or that inner planets become misaligned due to the torque from a wider-orbiting and misaligned giant planet (Lai et al. 2018). To decide among these and other theories will require a larger and more diverse sample of planetary systems for which the stellar obliquity can be probed.

We thank an anonymous referee for a careful reading of the earlier manuscript and also for numerous valuable comments. We are grateful to T. Campante for help in tracking down the reason for the discrepancy with previously published results. The numerical computation was carried out on the DALMA cluster at New York University Abu Dhabi, and the PC cluster at the Center for Computational Astrophysics, National Astronomical Observatory of Japan. S.K. is supported by a Japan Society for Promotion of Science (JSPS) Research Fellowship for Young Scientists (No. 16J03121). Y.S. gratefully acknowledges the support from a Grant-in Aid for Scientific Research by JSPS No. 18H01247. Work by F.D. and J.N.W. was supported by the Heising-Simons Foundation. O.B. thanks the invitation program supported by Research Center for the Early Universe, the University of Tokyo. The present research was initiated during Y.S.’s visit at Princeton University supported by the JSPS Core-to-Core Program “International Network of Planetary Sciences”, and also performed in part under contract with the Jet Propulsion Laboratory (JPL) funded by NASA through the Sagan Fellowship Program executed by the NASA Exoplanet Science Institute.

REFERENCES

- | | |
|--|--|
| Angus, R., Morton, T., Aigrain, S.,
Foreman-Mackey, D., & Rajpaul, V.
2018, MNRAS, 474, 2094 | Appourchaux, T., Benomar, O.,
Gruberbauer, M., et al. 2012, A&A,
537, A134. https://doi.org/10.1051/
0004-6361/201118496 |
| Appourchaux, T., Michel, E., Auvergne,
M., et al. 2008, A&A, 488, 705 | Atchade, Y. F. 2006, ArXiv Mathematics
e-prints, math/0605452 |

- Ball, W. H., & Gizon, L. 2014, *A&A*, 568, A123
- Batygin, K. 2012, *Nature*, 491, 418
- Benomar, O., Masuda, K., Shibahashi, H., & Suto, Y. 2014, *PASJ*, 66, 94
- Berger, T. A., Huber, D., Gaidos, E., & van Saders, J. L. 2018, *ApJ*, 866, 99
- Borucki, W. J., Koch, D., Basri, G., et al. 2010, *Science*, 327, 977
- Bourrier, V., Lovis, C., Beust, H., et al. 2018, *Nature*, 553, 477
- Campante, T. L., Lund, M. N., Kuszlewicz, J. S., et al. 2016, *ApJ*, 819, 85
- Christensen-Dalsgaard, J., & Thompson, M. J. 1997, *MNRAS*, 284, 527
- Davies, G. R., Silva Aguirre, V., Bedding, T. R., et al. 2016, *MNRAS*, 456, 2183
- Feroz, F., Hobson, M. P., & Bridges, M. 2009, *MNRAS*, 398, 1601
- Gizon, L., & Solanki, S. K. 2003, *ApJ*, 589, 1009
- Gregory, P. C. 2005, *Bayesian Logical Data Analysis for the Physical Sciences: A Comparative Approach with ‘Mathematica’ Support* (Cambridge University Press)
- Hansen, B. M. S., & Zink, J. 2015, *MNRAS*, 450, 4505
- Huber, D., Carter, J. A., Barbieri, M., et al. 2013, *Science*, 342, 331
- Jeffreys, H. 1961, *Theory of Probability*, 3rd edn. (Oxford, England: Oxford)
- Johnson, J. A., Petigura, E. A., Fulton, B. J., et al. 2017, *AJ*, 154, 108
- Kamiaka, S., Benomar, O., & Suto, Y. 2018, *MNRAS*, 479, 391
- Kjeldsen, H., Bedding, T. R., & Christensen-Dalsgaard, J. 2008, *ApJL*, 683, L175
- Lai, D., Anderson, K. R., & Pu, B. 2018, *MNRAS*, 475, 5231
- Lund, M. N., Lundkvist, M., Silva Aguirre, V., et al. 2014, *A&A*, 570, A54
- Mandel, K., & Agol, E. 2002, *ApJL*, 580, L171
- Marcy, G. W., Isaacson, H., Howard, A. W., et al. 2014, *ApJS*, 210, 20
- McQuillan, A., Mazeh, T., & Aigrain, S. 2013, *ApJL*, 775, L11
- Mosser, B., Michel, E., Belkacem, K., et al. 2013, *A&A*, 550, A126
- Nielsen, M. B., Schunker, H., Gizon, L., Schou, J., & Ball, W. H. 2017, *A&A*, 603, A6
- Petigura, E. A., Howard, A. W., Marcy, G. W., et al. 2017, *AJ*, 154, 107
- Petrovich, C., Deibert, E., & Wu, Y. 2018, *ArXiv e-prints*, arXiv:1804.05065
- Schlaufman, K. C. 2010, *ApJ*, 719, 602
- Sonoi, T., Samadi, R., Belkacem, K., et al. 2015, *A&A*, 583, A112
- Southworth, J. 2011, *ArXiv e-prints*, arXiv:1108.2976
- Suto, Y., Kamiaka, S., & Benomar, O. 2018, submitted
- Tassoul, M. 1980, *ApJS*, 43, 469
- . 1990, *ApJ*, 358, 313
- Thompson, S. E., Coughlin, J. L., Hoffman, K., et al. 2018, *ApJS*, 235, 38
- Toutain, T., & Gouttebroze, P. 1993, *A&A*, 268, 309
- Triaud, A. H. M. J. 2017, *The Rossiter–McLaughlin Effect in Exoplanet Research*, 2
- Triaud, A. H. M. J., Collier Cameron, A., Queloz, D., et al. 2010, *A&A*, 524, A25
- Van Eylen, V., Albrecht, S., Huang, X., et al. 2018, *ArXiv e-prints*, arXiv:1807.00549
- Winn, J. N., Fabrycky, D., Albrecht, S., & Johnson, J. A. 2010a, *ApJL*, 718, L145
- Winn, J. N., & Fabrycky, D. C. 2015, *ARA&A*, 53, 409
- Winn, J. N., Johnson, J. A., Howard, A. W., et al. 2010b, *ApJL*, 723, L223
- Winn, J. N., Sanchis-Ojeda, R., Rogers, L., et al. 2017, *AJ*, 154, 60
- Yee, S. W., Petigura, E. A., Fulton, B. J., et al. 2018, *AJ*, 155, 255